The Astrophysical Journal, 867:3 (11pp), 2018 November 1 https://doi.org/10.3847/1538-4357/aae317
© 2018. The American Astronomical Society.
OPEN ACCESS

Identifying Anticyclonic Vortex Features Produced by the Rossby Wave Instability in Protoplanetary Disks

Pinghui Huang[1,2,3], Andrea Isella[4], Hui Li[3], Shengtai Li[3], and Jianghui Ji[1]
[1] CAS Key Laboratory of Planetary Sciences, Purple Mountain Observatory, Chinese Academy of Sciences, Nanjing 210008, People's Republic of China; phhuang@pmo.ac.cn
[2] University of Chinese Academy of Sciences, Beijing 100049, People's Republic of China
[3] Theoretical Division, Los Alamos National Laboratory, Los Alamos, NM 87545, USA
[4] Department of Physics & Astronomy, Rice University, 6100 Main Street, Houston, TX 77005, USA
Received 2018 June 3; revised 2018 September 12; accepted 2018 September 18; published 2018 October 25

Abstract

Several nearby protoplanetary disks have been observed to display large-scale crescents in the (sub)millimeter dust continuum emission. One interpretation is that these structures correspond to anticyclonic vortices generated by the Rossby wave instability within the gaseous disk. Such vortices have local gas overdensities and are expected to concentrate dust particles with a Stokes number around unity. This process might catalyze the formation of planetesimals. Whereas recent observations showed that dust crescents are indeed regions where millimeter-size particles have abnormally high concentration relative to the gas and smaller grains, no observations have yet shown that the gas within the crescent region counterrotates with respect to the protoplanetary disk. Here we investigate the detectability of anticyclonic features through measurement of the line-of-sight component of the gas velocity obtained with ALMA. We carry out 2D hydrodynamic simulations and 3D radiative transfer calculations of a protoplanetary disk characterized by a vortex created by the tidal interaction with a massive planet. As a case study, the disk parameters are chosen to mimic the IRS 48 system, which has the most prominent crescent observed to date. We generate synthetic ALMA observations of both the dust continuum and ^{12}CO emission around the frequency of 345 GHz. We find that the anticyclonic features of the vortex are weak but can be detected if both the source and the observational setup are properly chosen. We provide a recipe for maximizing the probability of detecting such vortex features and present an analysis procedure to infer their kinematic properties.

Key words: hydrodynamics – instabilities – line: profiles – planet–disk interactions – protoplanetary disks – submillimeter: planetary systems

1. Introduction

Protoplanetary systems such as IRS 48 (van der Marel et al. 2013), LkHα 330 (Isella et al. 2013), HD 142527 (Muto et al. 2015), MWC 758 (Isella et al. 2010), and SAO 206462 (Pérez et al. 2014) exhibit large cavities and prominent crescents in the (sub)millimeter dust continuum emission. In systems where spatially resolved multiwavelength observations of both dust and gas emission exist, namely IRS 48, HD 142527, and MWC 758, the continuum crescents appear to originate from the azimuthal and radial concentration of solid particles toward local maxima of the gas pressure (Casassus et al. 2015; van der Marel et al. 2015; Boehler et al. 2017). Such concentration is believed to result from the decoupling between dust and gas and subsequent migration of solid particles in the direction of the gas pressure gradient (see, e.g., Weidenschilling 1977; Birnstiel et al. 2013). This interpretation is supported by the fact that gas–dust decoupling is most efficient for grains with a Stokes number around unity, which, for typical densities of protoplanetary disks, indeed correspond to grains that emit mostly at (sub)millimeter wavelengths.

Whereas the motion of dust particles in gaseous disks is relatively well understood, the origin of gas pressure maxima is not. A commonly accepted explanation for the existence of asymmetric pressure maxima in protoplanetary disks is that they originate from large-scale vortices resulting from hydrodynamic instabilities. Specifically, vortices can be generated by planets (Li et al. 2005; Fu et al. 2014b; Zhu et al. 2014) or viscosity transitions (Regály et al. 2013; Miranda et al. 2017). A massive planet or sharp radial viscosity transition creates a steep radial gradient in the gas density that triggers the Rossby wave instability (RWI; Lovelace et al. 1999; Li et al. 2000), which at the nonlinear stage can produce large-scale vortices (Li et al. 2001, 2005; Ou et al. 2007). Numerical simulations show that the formation and evolution of a vortex strongly depend on the disk viscosity. In particular, a vortex can form and survive for hundreds to thousands of orbits only if the viscosity is low ($\alpha \simeq 10^{-3} \sim 10^{-5}$; Fu et al. 2014a). Taken at face value, this result is in conflict with the typical $\alpha \simeq 0.01$ required to explain the mass accretion rates found in protoplanetary disks (Hartmann et al. 1998). However, theoretical models suggest that disk viscosity might vary with distance from the star, and that the innermost disk regions (<1 au), those responsible for accretion onto the star, might be more viscous than the disk regions probed by current spatially resolved observations (>10 au). Lacking direct measurements (but see Flaherty et al. 2017), the level of viscosity in protoplanetary disks remains highly debated.

In addition to informing us about disk viscosity, vortices might be pivotal in the formation of planets: they can speed up the dust coagulation and formation of planetesimals (Barge & Sommeria 1995), stop the radial inward drift of dust particles (Weidenschilling 1977), and help overcome the fragmentation

Original content from this work may be used under the terms of the Creative Commons Attribution 3.0 licence. Any further distribution of this work must maintain attribution to the author(s) and the title of the work, journal citation and DOI.

barrier (Brauer et al. 2008). Vortices generated at the edges of low-ionization regions could perhaps lead to the formation of the planetesimals needed by the core accretion model (Pollack et al. 1996) to form giant planets. Moreover, vortices generated by giant planets could perhaps control the formation and migration of rocky planets in their region of influence (see, e.g., Liu et al. 2018). Studying the presence of vortices in protoplanetary disks is therefore important to understand the architecture of the solar system and the multitude of planetary systems discovered so far.

In this paper, we study the direct detectability of vortices from spatially and spectrally resolved observations of the molecular-line emission at millimeter wavelengths. Observations of dust continuum crescents support the vortex hypothesis and, when combined with molecular-line data, provide an indication of the efficiency of the dust concentration process. However, direct measurements of the gas vorticity are necessary to (i) confirm that the observed dust crescents correspond to gas vortices and (ii) study the mechanisms related to the vortex formation and evolution. Here we focus on the scenario in which a vortex is created by a massive planet and simulate its density and velocity structure through high-resolution 2D hydrodynamic calculations of the disk–planet interaction. We then perform radiative transfer calculation to generate synthetic images of the dust and CO emission and process them through the ALMA simulator to properly account for observational noise. Synthetic observations are then analyzed to search for the signature of the vortex in the intensity moments of the gas intensity. We find that kinematic signatures of a vortex in a disk like IRS 48 can be detected by ALMA. We provide the observational setup required to achieve such a detection. Our analysis is complementary and extends the recent study of the effect of planet–disk interaction on the CO line emission presented by Pérez et al. (2018). Note that our analysis should be applicable to vortices excited via different mechanisms as described above, because the typical velocity variations associated with vortices are similar, with their magnitudes reaching a fraction of the local sound speed (Li et al. 2001).

The outline of this paper is as follows. In Section 2, we describe our numerical model setup and methods. In Section 3, we present the results of the numerical simulations and the synthetic images obtained. In Section 4, we discuss and summarize our results.

2. Modeling Procedure

2.1. Planet–disk Interaction Model

We use the two-fluid hydrodynamic 2D code LA-COMPASS (Li et al. 2005, 2008; Fu et al. 2014b) to simulate the formation and evolution of a large-scale vortex in a protoplanetary disk caused by interaction with a massive planet. The hydrodynamic model is initialized using properties similar to those of the IRS 48 system, though our results apply to protoplanetary disks in general. We adopt a stellar mass $M_\star = 2\,M_\odot$ (van der Marel et al. 2013) and a stellar effective temperature $T_\star = 9400$ K (Follette et al. 2015). The initial gas surface density profile is $\Sigma_{\rm gas}(r) = \Sigma_{\rm gas,0}(r/r_0)^{-1}$, where $\Sigma_{\rm gas,0} = 1.73\,{\rm g\,cm^{-2}}$ and $r_0 = 35$ au. The inner and outer boundaries of the disk are $0.4r_0 = 14$ and $6.68r_0 = 233.8$ au, respectively. Modeling by Bruderer et al. (2014) indicated that the inner gaseous disk of IRS 48 is depleted between 0.4 and 20 au. Here we have chosen the initial inner gas disk boundary at 14 au, and, with disk–planet interaction, the inner gas disk will be significantly depleted over time. Overall, we find that our results on vortices do not depend on the choice of the inner disk boundary. At the beginning of the simulation, gas and dust are well coupled with a gas-to-dust ratio of 100. Dust grains are modeled as compact spheres with a diameter of $s_{\rm d} = 0.20$ mm and internal density of $\rho_{\rm d} = 1.2\,{\rm g\,cm^{-3}}$. The corresponding Stokes number at r_0 is 0.022. The choice of the grain size has little effect on our results and is motivated by the fact that these are the grains that emit most of the thermal radiation observed at $\lambda = 2\pi s_d \approx 1$ mm. In particular, we find that our specific choice of 0.2 mm grain size does not affect the gas density and kinematics of the vortex.

Following the results of van der Marel et al. (2013), we introduce a 10 $M_{\rm J}$ mass planet at $r_0 = 35$ au from the star, so that $\mu = M_{\rm p}/M_* = 5 \times 10^{-3}$ and the planet orbital period equals about 146 yr. We perform hydrodynamic simulations by assuming a locally isothermal equation of state, where the radial profile of the temperature is $T(r) = T_0(r/r_0)^{-1/2}$ and the corresponding radial profile of the sound speed is $c_s = c_{s,0}(r/r_0)^{-1/4}$, with $c_{s,0} = \Omega_0 h_0$, $h_0 = 0.085 r_0$, and $\Omega_0 = \sqrt{GM_\star/r_0^3}$. This assumed disk temperature is consistent with that derived from the radiative transfer calculation discussed in the next section. We adopt a 2D uniform polar grid with 3072 cells in both the radial and azimuthal directions. Each cell therefore has a radial size of about 0.07 au, or $h_0/30$. We adopt a Shakura–Sunyaev viscosity α parameter of 7×10^{-5} (Shakura & Sunyaev 1973), which is the optimal value for generating vortices (Fu et al. 2014a). In this paper, we do not consider the feedback of dust on the vortex structure (Fu et al. 2014b) or the planet migration. The viscous heating is also neglected in our simulation because the viscous dissipation rate $D(R) = \frac{9}{8}\nu\Sigma\frac{GM}{R^3}$ (Frank et al. 2002; Chiang & Youdin 2010), where Σ is the gas surface density of the disk. If the disk radiates as a blackbody, $\sigma T^4 = D(R)$, the fluctuation of temperature caused by the viscous heating is small, so we can ignore the viscous heating even at the vortex region.

Figure 1 shows the surface density profile of gas and dust in our two-fluid hydrodynamic simulations after 720 orbits of the planet, or about 10^5 yr. The planet carves a deep circular gap in the gas distribution from about 25 to 45 au (left panel). At the outer edge of the gap, the gas surface density sharply increases by more than a factor of 10 within 5 au. This sharp increase causes the formation of a vortex that extends radially from 55 to 75 au and azimuthally from 163° to 251° (0° is along the x-axis direction). The center of the vortex is located about 65 au from the central star and at an azimuthal angle of 207°.

The dust distribution is strongly affected by the planet as well. It features a circular gap that is much wider than that in the gas and extends out to a radius of about 85 au, i.e., well beyond the location of the vortex. Within this gap, our model predicts a strong accumulation of dust caused by the radial and azimuthal trapping of solid particles toward the center of the vortex. As a result of the disk–planet interaction and dust migration toward gas pressure maxima, the dust-to-gas ratio increases by about a factor of 10 at the outer edge of the dust gap and almost a factor of 100 within the vortex. Whereas at the center of the vortex, the model predicts a dust-to-gas ratio close to unity, it is important to note that this value is likely overestimated due to the lack of dust feedback that might quench the concentration of solid particles (Fu et al. 2014b).

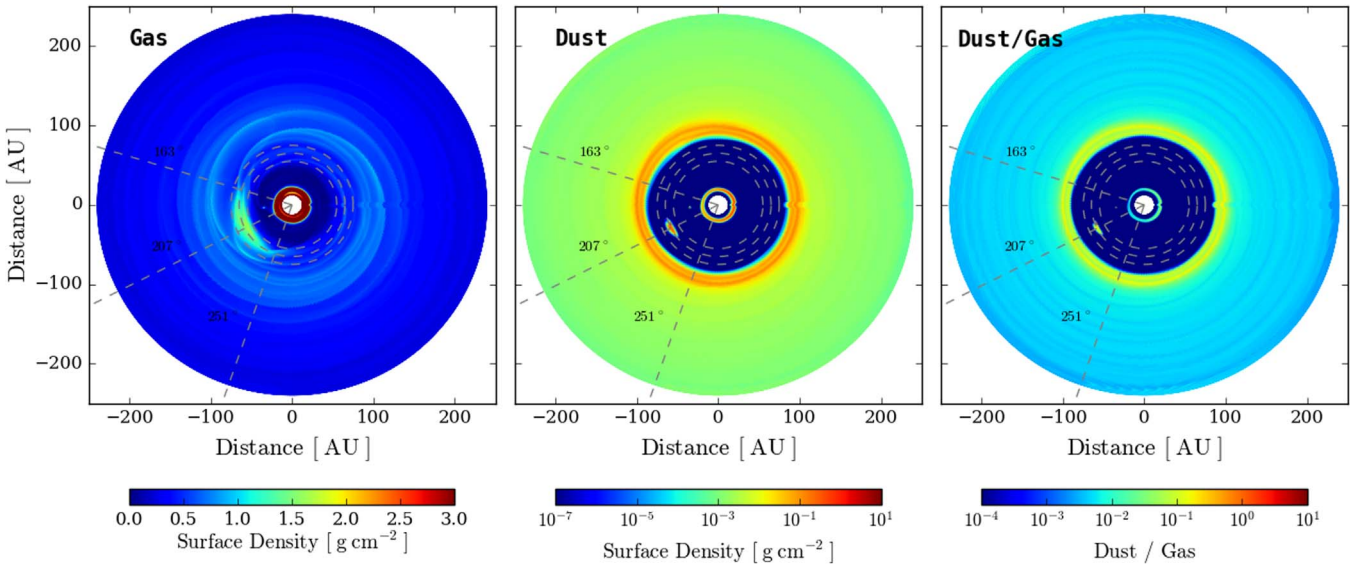

Figure 1. Snapshot of the surface density of the gas (left) and dust (center) of a disk perturbed by a 10 M_J planet orbiting at 35 au from a 2 $M_\odot$ star at 10^5 yr. The planet–disk interaction leads to the formation of a vortex centered at 65 au from the central star at a position angle of 207°. The vortex extends azimuthally from 163° to 251° and radially from 55 to 75 au. The vortex region in the density profile is marked by the dashed lines and dashed circles, which indicate radii of 55, 65, and 75 au, respectively. The right panel shows the dust-to-gas surface density ratio. Planet–disk interaction leads to an enhancement of dust density both within the vortex and at the outer edge of the gap created by the planet.

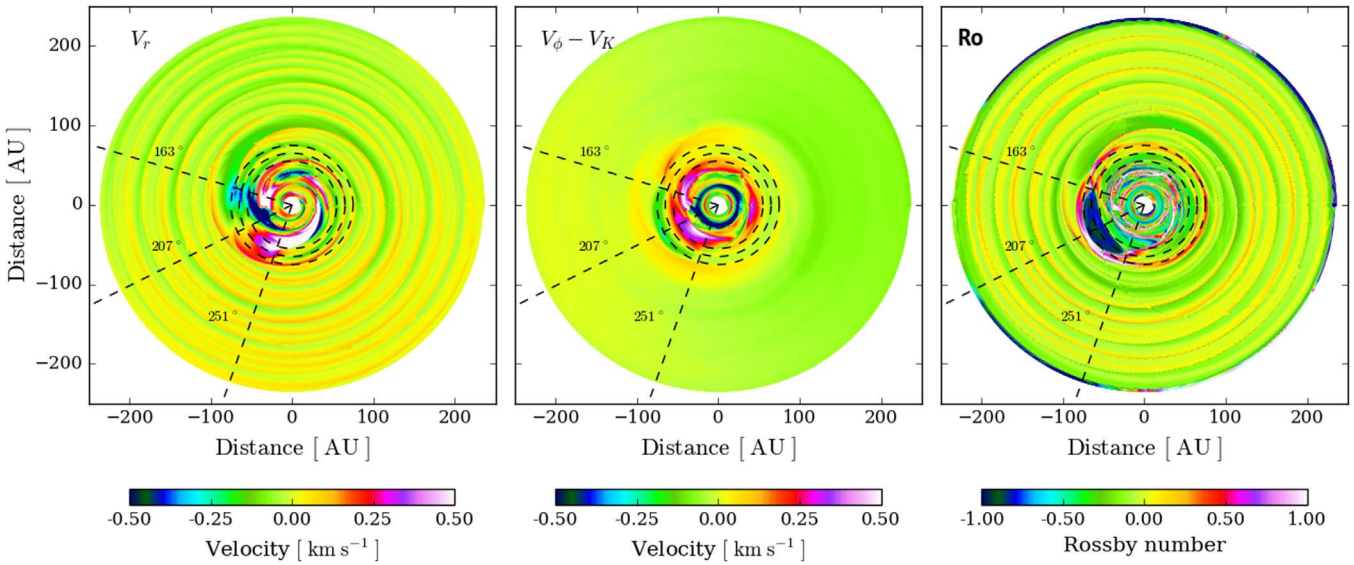

Figure 2. Radial (left) and azimuthal (center) components of the gas velocity. The vortex appears as an anticyclone (clockwise rotation) and a region characterized by negative values of the Rossby number (right). In the central panel, the Keplerian velocity has been subtracted from the gas velocity to better display the perturbations caused by the planet. For reference, the Keplerian velocity at 35 au is 7.12 km s^{-1}.

Figure 2 shows the gas velocity v_g along the r and ϕ directions relative to the Keplerian motion v_K, as well as the Rossby number of the gas, $\mathrm{Ro} = 2[\nabla \times (v_g - v_K)]_z/\Omega_K$. The main perturbation induced by the planet is an anticyclonic rotation (clockwise, $\mathrm{Ro} < 0$) centered at the position of the vortex and extending azimuthally for almost one-fourth of the disk between about 160° and 250°. In this region, the radial and azimuthal velocity of the gas varies between ± 0.5 and ± 0.3 km s^{-1}, respectively. The velocity deviations from Keplerian motion are comparable to the local sound speed and, as discussed in Li et al. (2001), might produce shocks capable of forming spiral density waves themselves. For the purpose of this paper, a key aspect is that the velocity perturbations associated with the vortex are sufficiently large to be detected with spatially resolved spectroscopic observations of molecular-line emission from protoplanetary disks. The detectability of the kinematic signatures of a vortex and, in general, of the planet–disk interaction, is discussed in the following sections.

2.2. Obtaining Disk Temperature Distributions

We use the radiative transfer code RADMC-3D (Dullemond 2012) to calculate the temperature and emission of the disk perturbed by the planet following a procedure similar to that described in Jin et al. (2016). In brief, we first convert the 2D gas surface density distribution generated by LA-COMPASS into a 3D

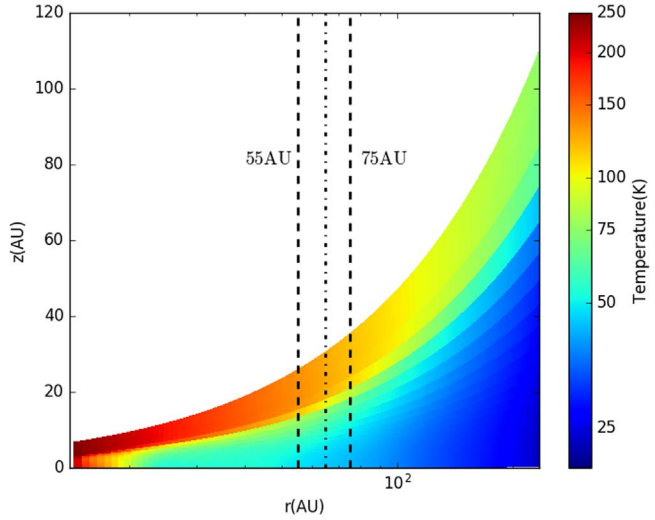

Figure 3. Azimuthally averaged disk temperature obtained through 3D radiative transfer calculations. The inner and outer radii of the vortex are marked by the dashed lines. The radial location (65 au) of the vortex center is marked by the dot-dashed line.

cylindrical density structure defined as $\rho(r, \phi, z) = \frac{\Sigma(r,\phi)}{\sqrt{2\pi}h(r)} e^{\frac{-z^2}{2h(r)^2}}$, where, as above, $h(r) = c_s(r)/\Omega(r) = h_0(r/r_0)^{5/4}$. Since the disk opacity at the wavelengths at which disk heating and cooling occur (i.e., optical and infrared) is controlled by (sub) micron grains that are coupled to the gas, it is appropriate to use the gas density for the calculation of the disk temperature. To calculate the disk temperature, we assume a disk opacity proper of interstellar dust made of astronomical silicates (Weingartner & Draine 2001), organic carbonates (Zubko et al. 1998), and water ice, with fractional abundances as in Pollack et al. (1994) and a grain size distribution $n(a) \propto a^{-3.5}$ between 0.01 and 1 μm. We instead include grains as large as 1 mm to calculate the millimeter-wave dust emission. In both cases, the gas-to-dust ratio is set to 100. We then perform a radiative transfer Monte Carlo simulation, which leads to a Monte Carlo noise on the disk midplane temperature below 3%, as required to properly solve for the hydrostatic equilibrium (see, e.g., Isella & Turner 2018). Since the disk density and temperature are mutually dependent, a few iterations are required to reach a stable solution. We find that the disk reaches stable hydrostatic and thermal equilibrium at a midplane temperature $T(r) \approx 73\ \mathrm{K}(r/r_0)^{-1/2}$, or $h(r) = 0.085(r/r_0)^{5/4}$. The disk temperature is to the first approximation azimuthally constant (Figure 3), although the higher gas and dust density at the vortex causes small azimuthal temperature variations (by a few degrees) whose effects might be difficult to detect. A more detailed discussion on the radial and azimuthal temperature perturbation caused by the disk–planet interaction can be found in Isella & Turner (2018).

We note that the 3D disk temperature obtained via RADMC-3D gives the typical two-layered structure shown in Figure 3 (e.g., Chiang & Goldreich 1997). The radial temperature profile in the midplane, however, is lower than the initial temperature profile used in the 2D hydrodynamical simulations by about 20%–30%. Furthermore, because the 3D disk temperature distributions were obtained via postprocessing radiative transfer calculations, these quantities are presumably not self-consistent with the realistic dynamic radiation hydrodynamic calculations. The exact impact of these simplifications will need to be understood in future studies.

2.3. Synthetic Images and Mock-up ALMA Observations

Once the disk temperature is set, we calculate the synthetic disk emission in the ^{12}CO $J = 3$–2 line emission at 345.796 GHz and in the surrounding dust continuum emission. To calculate the dust emission, we assume that millimeter grains are settled toward the midplane with respect to the gas. Their vertical distribution is assumed to be Gaussian with a pressure scale height $h_{\mathrm{dust}}(r) = 0.1h(r)$ (Isella et al. 2016; Pinte et al. 2016). The CO emission is calculated assuming local thermodynamic equilibrium (LTE; see, e.g., Weaver et al. 2018 for a discussion of the applicability of LTE to protoplanetary disks) and a fractional abundance $\chi(^{12}\mathrm{CO}) = 1.4 \times 10^{-4}$ relative to H_2. The Doppler shift of the line emission is calculated using the gas velocity v_g provided by the hydrodynamic simulation discussed above (see Figure 2). The spectral profile of the emission line is calculated accounting only for thermal broadening; i.e., no turbulence is included in the model. This choice is motivated by the low values of turbulence measured in some protoplanetary disks (Flaherty et al. 2017, 2018; Teague et al. 2018). We generate synthetic images for disk inclinations of 25° and 50° in a velocity interval of $\pm 7\ \mathrm{km\ s^{-1}}$.

As the final step in our modeling procedure, we use the simobserve task in the Common Astronomy Software Applications package (CASA[5]; McMullin et al. 2007) to generate mock-up ALMA observations that account for the effect of finite angular resolution and sensitivity. Our goal is to investigate the detectability of the kinematic signatures of the vortex in the line emission and the factors that affect such signatures. Since the vortex has a spatial extent of approximately 30 au, or 0.″25, at a source distance of 120 pc, we adopt an array configuration that provides an FWHM beam size of about 0.″1 with natural weighting (CASA antenna file number 17). Lower-resolution images would not spatially resolve the vortex, while observing the CO emission at higher resolution with good sensitivity would require very long observations.

The azimuthal position of the vortex is important because observations of the line emission measure the component of gas velocity along the line of sight. As a consequence, if the vortex is located along the apparent minor axis of the disk ($\theta = 90°$), the v_ϕ component of the gas velocity will mostly be perpendicular to the line of sight and will not generate any Doppler shift. In this model, the kinematic signature of the vortex would depend on the radial component of the gas velocity. Vice versa, when the vortex is close to $\theta = 180°$, its observable kinematic signature will depend on v_ϕ, while the v_r component along the line of sight would be close to zero. As such, we generate mock-up observations by rotating the synthetic models so that the vortex is close to either the projected minor axis of the disk ($\theta = 128°$) or its major axis ($\theta = 198°$ and 205°).

Besides the angular resolution of the observations and the location of the vortex, the detectability of the vortex kinematics would depend on the sensitivity and velocity resolution of the observations. Here we generate mock-up observations that provide velocity resolutions of 0.1 and $0.05\ \mathrm{km\ s^{-1}}$ and sensitivities between 3.5 and 5.5 K.

[5] https://casa.nrao.edu/

Table 1
Model Parameters of the Synthetic ALMA Observations

Model	Inclination	Position Angle of Center of Vortex	Integration Time	Velocity Resolution
A (standard run)	50°	198°	2 hr	0.1 km s^{-1}
B	25°	205°	2 hr	0.1 km s^{-1}
C	50°	128°	2 hr	0.1 km s^{-1}
D	50°	198°	4 hr	0.1 km s^{-1}
E	50°	198°	4 hr	0.05 km s^{-1}

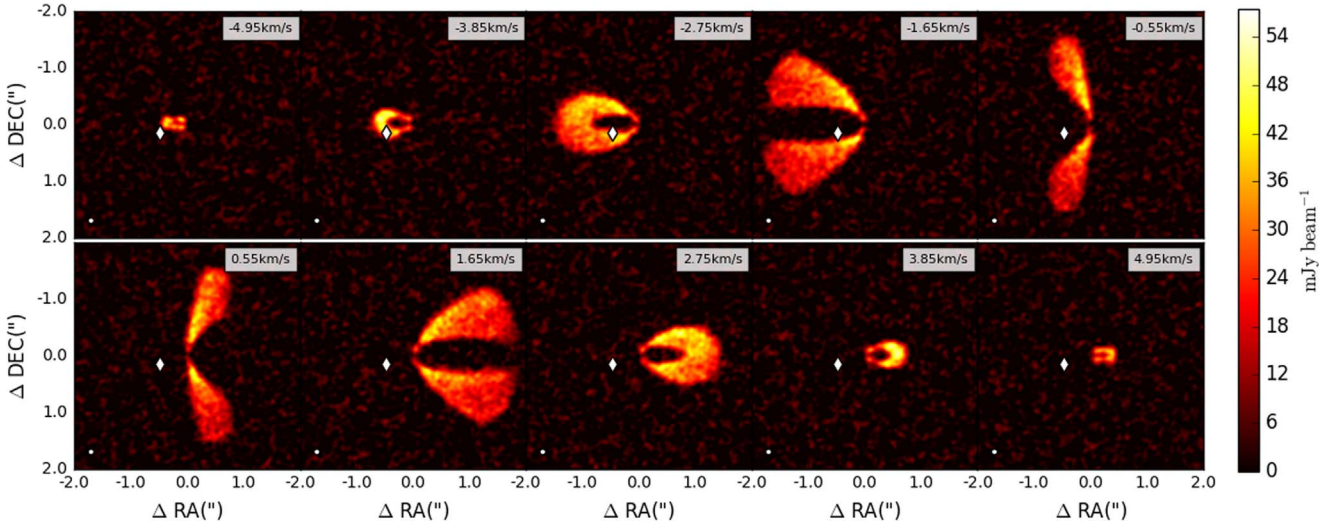

Figure 4. Subset of the mock-up channel maps of the ^{12}CO $J = 3$–2 line emission for model A. The position of the vortex is indicated with a diamond, while the size of the synthesized beam is marked as a white ellipse in each panel. Our model covers a velocity interval from −7.0 to 7.0 km s^{-1} at 0.1 km s^{-1} velocity resolution, for a total of 140 channels. The x and y axes show the offsets relative to the central star, which is located at (0, 0).

In total, we generated a set of five mock-up observations whose observational parameters are listed in Table 1. Each mock-up observation consists of an image of the dust continuum and a continuum-subtracted channel map of the ^{12}CO emission.

A subset of ^{12}CO channel maps for model A is shown in Figure 4, while spatially integrated spectra for all models are presented in Figure 5. The peak of the line emission is optically thick ($\tau_{\rm co} > 500$) across most of the disk, including the vortex, while the dust emission reaches an optical depth of about 5 only at the center of the vortex. The line spectra present the characteristic double-peak shape caused by the disk rotation. The line emission of model B is narrower and more intense because of the smaller inclination. In general, the blueshifted peaks have slightly higher intensities than the redshifted peaks. As discussed in the next section, this is caused by the enhanced gas surface density in the vortex region. It is worth mentioning that we have also investigated the observability of the vortex in the ^{13}CO $J = 3$–2 line, but, given the much lower signal-to-noise ratio of the simulated observations (or the much longer telescope time required to achieve the same signal-to-noise ratio of ^{12}CO observations), they do not provide any advantage in detecting the kinematic signature of the vortex and therefore are not discussed here.

In addition to channel maps and spatially integrated spectra, we produced images of the zeroth, first, and second moment of the line emission, corresponding to the spectrally integrated line intensity, intensity-weighted velocity centroid, and intensity-weighted line width, respectively. These maps are shown in Figure 6, together with the image of the dust continuum emission.

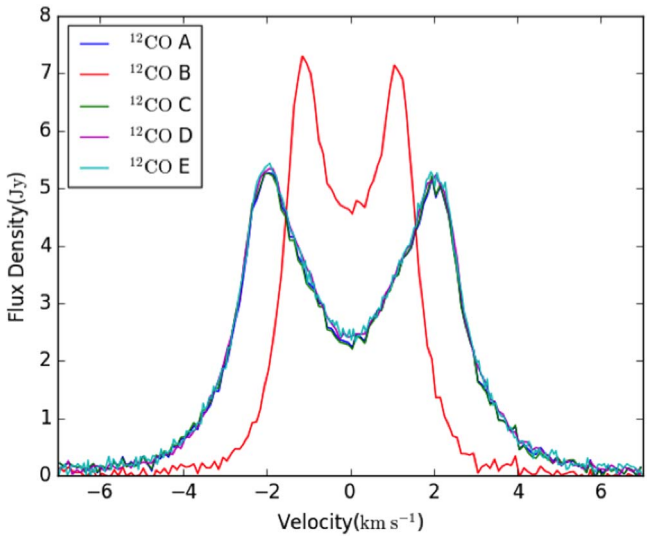

Figure 5. Spectra of the ^{12}CO $J = 3$–2 line emission integrated across the entire disk for all five models.

The center of the vortex in the moment maps is marked as the intersection between the dashed line and the dashed ellipse. The zeroth- and second-moment maps of ^{12}CO look like butterflies with cross-shaped features because the inclination of the disk lets the channels with larger velocity gradients along the line of sight have better relative velocity resolutions (Adam 1990).

In the following section, we discuss the observability of the vortex in each of these models.

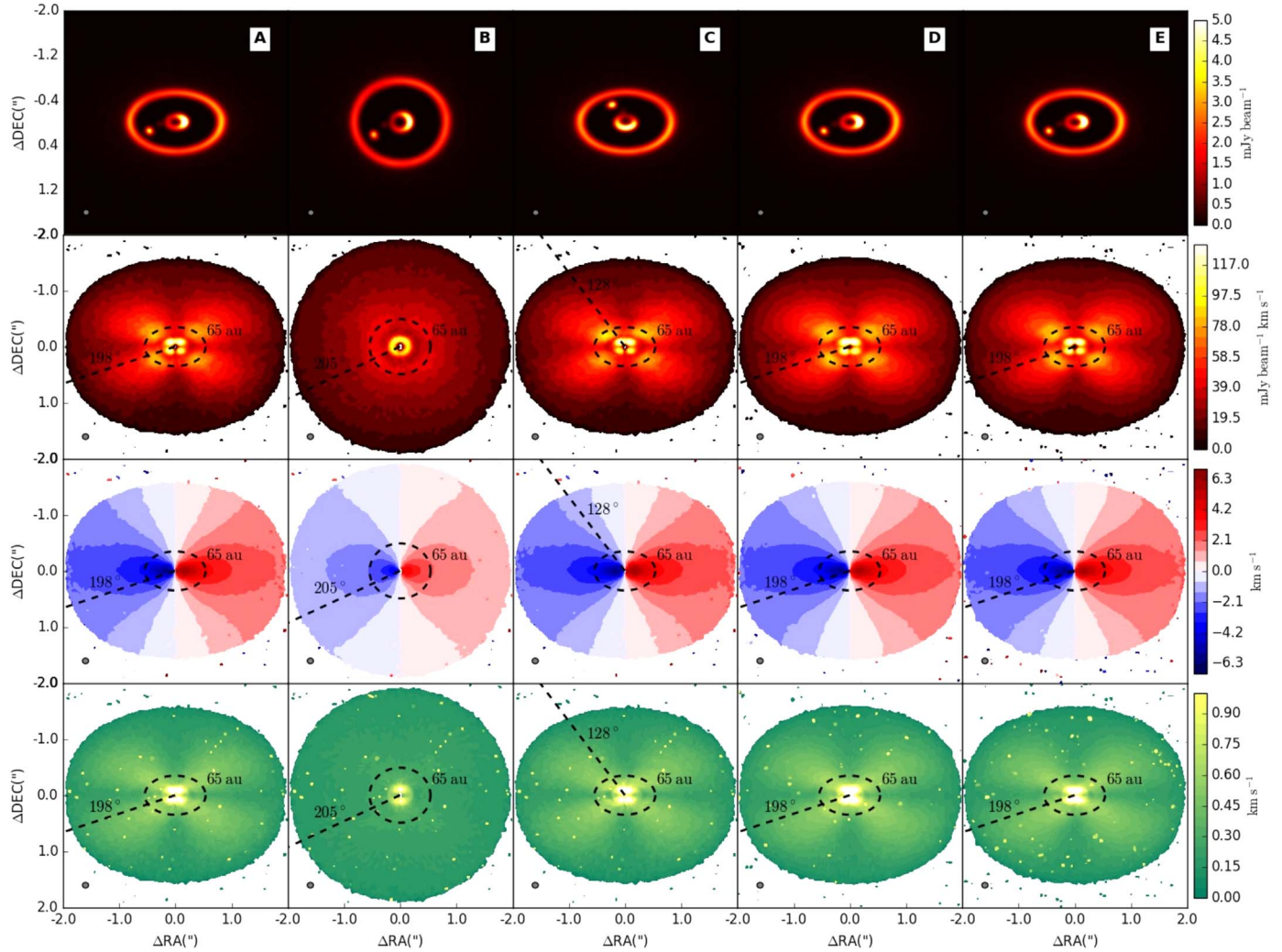

Figure 6. Dust continuum (345.796 GHz) and ^{12}CO $J = 3$–2 line emission moment maps for models A to E (columns). From top to bottom, each row presents the dust continuum, zeroth-moment, first-moment, and second-moment map of the gas intensity of each model, respectively. The size of the synthesized beam is shown as a gray ellipse at the bottom left corner of each panel. Where the dashed ellipse and the dashed line intercept marks the center of the vortex in each panel.

3. Kinematic Signature of the Vortex in ALMA Mock-up Observations

At first glance, Figures 4–6 do not show any obvious signature of the vortex in the molecular-line emission, despite the fact that it significantly perturbs the gas velocity. The first result of our investigation is therefore that vortices lead to rather small perturbations in the line emission and can hardly be identified by visually inspecting channel maps.

Here we search for the faint vortex signature based on the following idea. In the model of an unperturbed Keplerian disk, channel maps with the same absolute value of the radial velocity are symmetric with respect to the apparent minor axis of the disk (which corresponds to the projection of the angular moment vector on the plane of the sky). This means that, besides the opposite sign of the radial velocity, the blue- and redshifted sides of the disk should be similar. We can therefore search for kinematic perturbations from Keplerian rotation by folding the line emission along the disk minor axis and subtracting, pixel by pixel, the redshifted emission from the blueshifted line intensity. Figure 7 shows this procedure applied to the moment maps of the ALMA mock-up observations. Below, we discuss the signature of the vortex in each of the five models listed in Table 1.

3.1. Model A: Standard Run

In this model, the disk has an inclination of 50°, similar to IRS 48 (Geers et al. 2007), and the center of vortex is located at a position angle of 198°. The observations have a velocity resolution of 0.1 km s^{-1} and achieve a sensitivity of 5.2 K. In the zeroth-moment map of ^{12}CO, the intensity of the gas emission in the center of the vortex is lower than in the nearby region. This is in conflict with the fact that the surface density of the gas peaks at the center of the vortex (see Figure 1). This phenomenon was also reported by Boehler et al. (2017) in the HD 142527 CO gas line observations and is caused by the fact that the optically thick line emission arising from the disk surface absorbs the continuum emission originating from deeper layers of the disk. Continuum subtraction then leads to artificial removal of line emission (Boehler et al. 2018). When both dust and gas emission are optically thick (as happens at the center of the vortex), this situation become more severe, and continuum subtraction might result in the removal

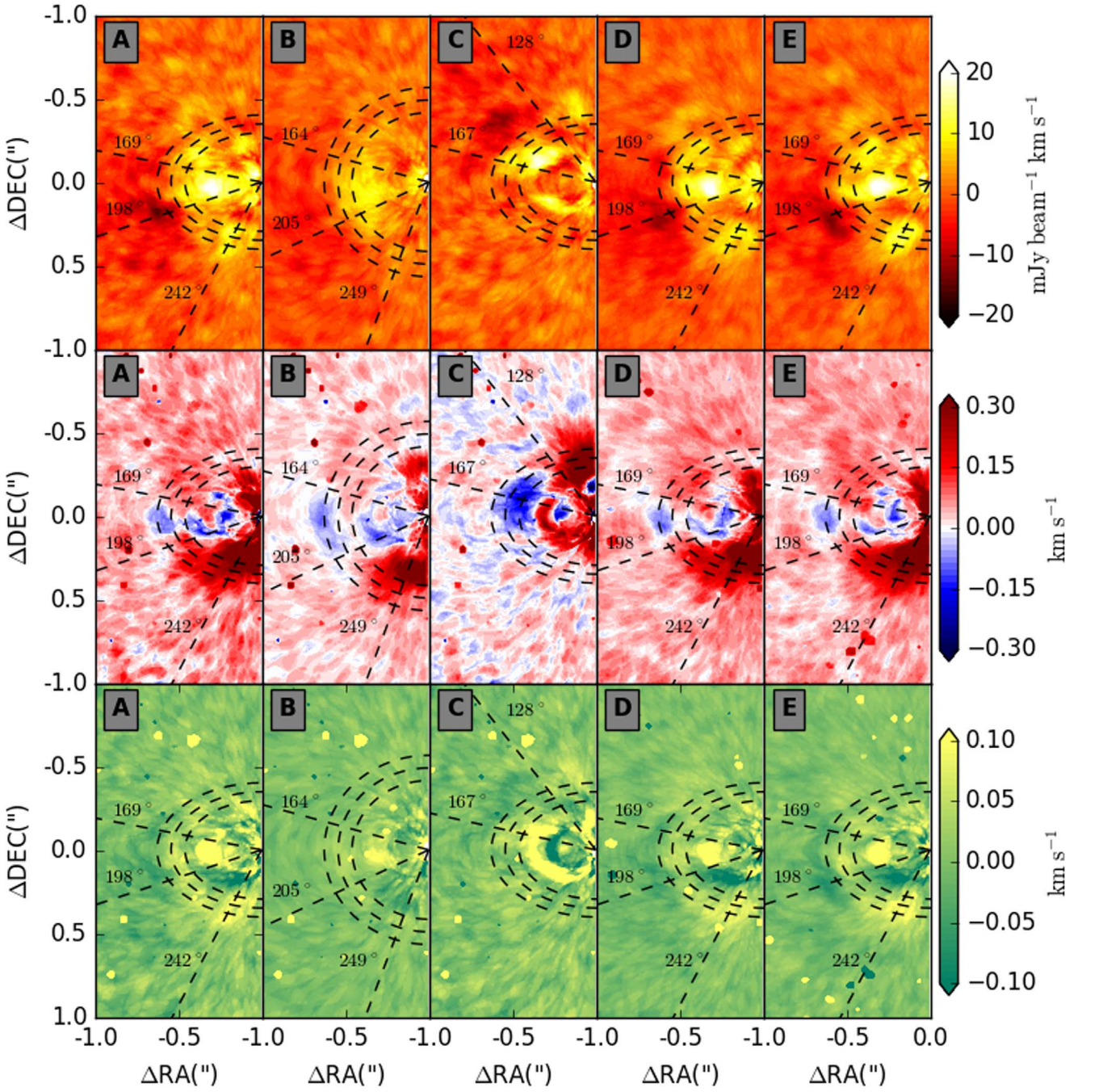

Figure 7. Top to bottom, left to right: Difference between the blueshifted side and the redshifted side of the zeroth, first, and second moment of the ^{12}CO $J = 3$–2 line emission for each model. The vortex regions are marked as the zones between the dashed ellipses and the dashed lines. The dashed ellipses from inside to outside indicate radii of 55, 65, and 75 au, same as Figure 1. The dashed lines mark the azimuthal position of the vortex in the moment maps. We can see that there are blue and red deviations compared with the background between 55 and 75 au in the middle row. These features are caused by the anticyclonic velocity field of a vortex.

of most of the line emission. In our model, however, the intensity of the ^{12}CO emission only drops slightly due to continuum subtraction, and the detectability of the vortex itself is not affected. We have tested this by generating images of the non-continuum-subtracted line emission. But since the results are very similar, we are not showing them here.

The difference between the blueshifted and redshifted sides of the zeroth-moment map of the ^{12}CO $J = 3$–2 line for model A is shown in the top row of Figure 7. The region enclosed by the dashed ellipses and dashed lines with position angles marks the region of the vortex. Reading from the top panel of model A, the difference is negative outside the radius of the vortex and positive inside. This is due to the fact that the gas and dust density enhancement within the vortex changes how the disk is illuminated by the star and, consequently, its temperature. In practice, the inner side of the vortex is more directly illuminated by the star, and it is slightly hotter than the unperturbed disk. Vice versa, the outer part of the vortex is illuminated at a more slanted angle and is slightly colder.

The kinematic signature of the vortex can be seen by looking at the difference between the blue- and redshifted sides of the first and second intensity moments. The vortex in the protoplanetary disk is an anticyclone, so it rotates clockwise, compared with the anticlockwise rotation of the whole disk.

This effect results in a detectable gradient in the velocity of the gas along the line of sight across the radial and azimuthal extent of the vortex. We can see that the blueshifted side of disk has a larger value of line-of-sight velocity than the redshifted side outside 75 au in all models, as shown by the second row of Figure 7, with the overall reddish background over the whole domain. (The implications of this effect will be explored in future studies.) On top of the reddish velocity difference background, however, there is a blue deviation ($\sim$0.1 km s^{-1}) between 55 and 75 au, 169° and 198°. This blue deviation is caused by the anticyclone vortex. A similar feature was also seen in the first-moment maps of models B, D, and E. In particular, gas located outward of the vortex center rotates slower than Keplerian, and its velocity along the line of sight is about -0.15 km s^{-1} lower than the velocity at the center of the vortex. Vice versa, gas located inside the radius of the vortex center rotates faster than Keplerian, and its line-of-sight velocity is about 0.15 km s^{-1} faster than that of the center of the vortex. As a result, the velocity gradient along the vortex is about 0.3 km s^{-1}, i.e., about three times bigger than the velocity resolution of the observations. Note that such a velocity gradient can manifest itself both in the radial and azimuthal directions.

The vortex also has a signature in the line width as described by the second moment of the line intensity, as shown in the bottom row of Figure 7. In this model, regions close to the center of the vortex have higher velocity dispersions that are caused by the fact that the observations do not spatially resolve the innermost part of the vortex, and therefore the emissions from gas regions moving at different velocities are all observed within one resolution element. At a resolution of 0.″1, this effect is, however, rather minor (the velocity dispersion increases by only 0.05 km s^{-1}).

In order to further illustrate how the velocity fields affect the moment maps, we run another five models, which are marked as A′ to E′. The surface density and temperature profile are kept the same as in models A–E, and we just changed the velocity input as a purely Keplerian velocity field when we generate the synthetic images using RADMC-3D. Detailed comparisons between Figures 7 and 8 show that (1) even though some generic features, such as the blue and red regions seen in the first-moment maps, are still visible in Figure 8, they are quite a bit weaker and not as systematic; and (2) features in the second-moment maps of Figure 8 become too weak to discern. These comparisons indicate that velocity fields containing a vortex made by a planet can indeed be "visibly" different from a purely Keplerian velocity field, lending further support to detecting such features in actual observations.

In conclusion, the combination of the perturbation signatures observed in the zeroth, first, and second moments can pinpoint the position of the vortex and yield the magnitude of its rotational velocity.

3.2. Model B: Effect of Disk Inclination

In model B, we lower the disk inclination from 50° to 25°. Because of the lower disk inclination, the disk is more circular and the gas velocity along the line of sight is smaller. As a result, the signature of the vortex in the gas moment maps becomes less significant than in model A. It is obvious that the blue and red deviations are less significant than those of model A ($\sim$0.75 km s^{-1}). Further lowering the disk inclination would lead to a very weak and undetectable kinematic signature of the vortex. In the limiting model of a face-on disk, the component of the gas rotational velocity along the line of sight vanishes, and the vortex becomes invisible. We compare the deviation of moment maps in B and B′ and find that it is hard to see the vortex features in B′ because of the low inclination and the Keplerian velocity field in B′. This confirms that the low inclination is not favorable to finding vortex features in the 2D hydrodynamic models. In reality, vortices might cause a vertical circulation of the gas, and they might be observed even at face-on inclination. However, exploring this scenario would require 3D hydrodynamic models. In the opposite situation, when the disk inclination is larger than 60°, the molecular-line emission arising from the inner disk regions might be blocked by the outermost flaring disk regions. This would also hamper the investigation of the vortex kinematics. Our analysis shows, therefore, that the best inclination range to detect kinematics signatures of the vortex spans between 30° and 60°.

3.3. Model C: Effect of the Azimuthal Position of the Vortex

Because observations measure the component of the gas velocity along the line of sight, the azimuthal position of the vortex with respect to the apparent minor axis of the disk has an effect on its observability. In particular, velocity perturbations with respect to the Keplerian motion of vortices located close to the disk major axis (PA $\sim$ 0°, 180°) are proportional to $V_\phi \sin(i)$, while velocity perturbations of vortices located close to the disk minor axis (PA $\sim$ 90°, 270°) depend on $V_r \sin(i)$, where V_ϕ and V_r are the tangential and radial velocities, respectively (Figure 2). In model C, we rotate the viewing angle so that the center of the vortex is at a position angle of 128°. Despite the fact that part of the vortex now extends into the redshifted part of the disk, its kinematic signature remains clearly visible in the first-moment difference. Actually, the amplitude of the velocity difference is larger compared to model A and has a variation of $\pm$0.25 km s^{-1}.

3.4. Model D: Effect of Thermal Noise

The thermal noise level of the observation is proportional to $1/\sqrt{t}$, where t is the observation time. To investigate the effect of thermal noise on the observations, in model D, we increase the integration time on source from 2 to 4 hr. The rms noise per channel consequently drops from 2.9 mJy beam^{-1} in model A to about 2.1 mJy beam^{-1}. Because the noise level has dropped by about 30%, the dust continuum and gas moment maps in model D achieve higher signal-to-noise and appear smoother compared to model A. However, the difference between the blueshifted and redshifted parts of the first and second moments changes only slightly. The comparison between D and D′ is similar to that between A and A′, just less noisy.

3.5. Model E: Effect of Velocity Resolution

In model E, we increase the velocity resolution from 0.1 to 0.05 km s^{-1}. Since the rms noise is proportional to $1/\sqrt{\Delta v}$, we extend the total observation time to 4 hr in order to compare with our standard run. The dust continuum and moment maps are shown in the fifth column of Figure 6, while the differences between the blueshifted and redshifted sides of the disk are presented in the fifth column of Figure 7. The comparison of E and E′ in Figures 7 and 8 is similar to that of A and A′. Overall,

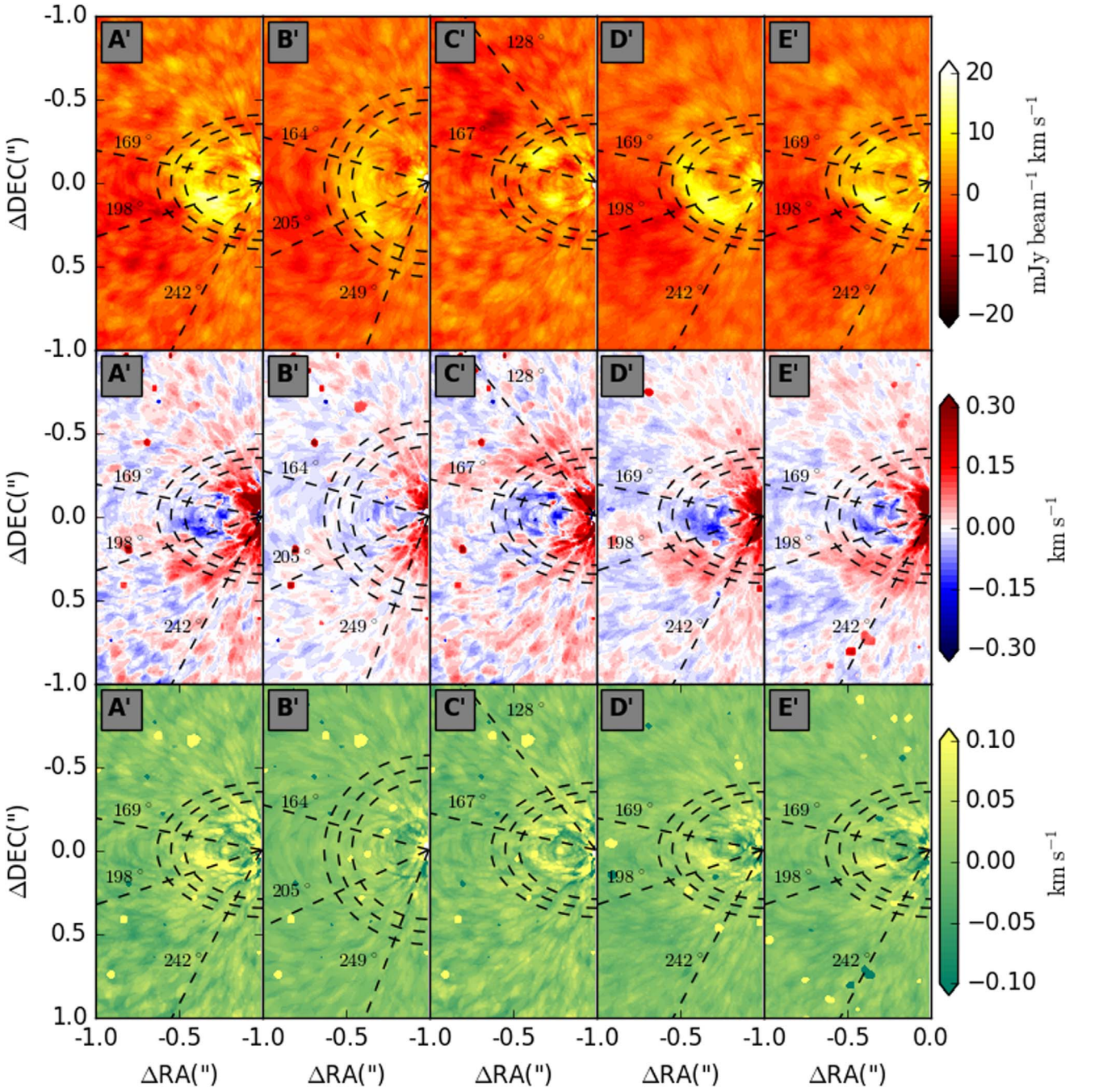

Figure 8. Same as Figure 7. The surface density and temperature profiles of A′–E′ are the same as those of A–E in Figure 7, but the velocity field input of RADMC-3D is now a purely Keplerian velocity field. Compared with Figure 7, the blue and red deviations between 55 and 75 au are much weaker in the middle row. Differences between the two figures indicate that the anticyclonic velocity field of a vortex can be observationally detected.

the kinematics signature of the vortex in model E is very similar to that observed in models A and D. The higher velocity resolution results in a smoother map of the second moment, but the improvement is marginal and perhaps not worth the longer integration time.

4. Discussion and Conclusions

ALMA observations have revealed azimuthal asymmetries in several protoplanetary disks that are thought to trace large-scale vortices produced by the RWI excited by planet–disk interactions. If this interpretation is correct, such vortices should perturb the motion of the gas and, consequently, the spectral profile of the gas emission from the affected regions. To investigate whether these perturbations could be detected, we have performed high-resolution 2D hydrodynamic and 3D radiative transfer simulations of a protoplanetary disk characterized by the presence of an anticyclonic vortex generated by the gravitational interaction between the disk and a 10 M_J planet located 35 au from the central star. The stellar and planet properties were chosen to roughly match those of the IRS 48 system, which is characterized by the most extreme azimuthal asymmetry discovered to date. The vortex traps the dust, as previously discussed by Fu et al. (2014a), and produces a compact azimuthal asymmetry characterized by an azimuthal

density variation larger than three orders of magnitude. As a reference, the azimuthal dust density variation measured in IRS 48 is larger than a factor of 100. By comparison, the gas density varies azimuthally only by about a factor of two (Figure 1). In addition to the dust trapping, the vortex induces variations in the gas velocity of the order of the gas sound speed (Figure 2), which can be probed by observing the molecular-line emission.

We used CASA to generate images of dust continuum and ^{12}CO $J = 3$–2 emission around the frequency of 345 GHz that could be observed in ALMA band 7. We chose this band because it provides the best sensitivity to thermal gas and dust emission. We explored the observability of the vortex kinematic signature by varying observational parameters such as the disk inclination and position angle, integration time, and velocity resolution.

Overall, we found that despite the rather large perturbations in the gas velocity (Figure 2), the signature of the vortex on the ^{12}CO line emission is weak, and it can be easily overlooked by visually inspecting the channel maps or intensity moments. This is due to the fact that (i) the azimuthal variation in the gas density at the radius of the vortex is much weaker than the azimuthal variation in the dust density and (ii) the ^{12}CO line is mostly optically thick and therefore only weakly depends on the gas density. Nevertheless, we show that the velocity perturbations due to the vortex can be recovered by comparing the blue- and redshifted sides of the disk. We find, in particular, that the rotation of the vortex is clearly visible by folding the first-moment map along the disk apparent minor axis and subtracting the blueshifted emission from the redshifted emission, or vice versa. This is a simple approach that does not require performing any detailed and time-consuming forward modeling.

In order to be more concrete, we have used the disk parameters of the IRS 48 system as a case study to investigate the detection feasibility by ALMA. By exploring different observational conditions, we established the following recipe to maximize the probability of directly detecting vortices in protoplanetary disks using ALMA observations.

1. To detect the kinematic signature of a vortex, it is necessary to spatially resolve it across a few resolution elements. Although a careful analysis of the spatially integrated line profile might also reveal velocity perturbations, our simulations show that the effect on spatially integrated spectra is generally too weak to be unambiguously attributed to a vortex. Given the angular size of the dust crescents observed so far, we find that the observations should achieve an angular resolution of about $0\farcs1$, corresponding to spatial scales of about 10–20 au at the distance of nearby star-forming regions.
2. To measure the velocity gradient across the vortex, the observations should detect the line emission with a peak signal-to-noise ratio larger than 15. Because the temperature of protoplanetary disks at a few tens of au from the central star ranges between 20 and 100 K, the observations should achieve a brightness temperature sensitivity of 1–7 K if the line under consideration is optically thick and fills the beam entirely (i.e., there is no beam dilution). Achieving such a sensitivity with a beam size of $0\farcs1$ and a velocity resolution of 0.1 km s^{-1} would require between about 1 (to reach an rms of 7 K) and 48 (to reach an rms of 5 K) hr of integration time on source with ALMA. Observing disks around hot stars is therefore highly preferable. Furthermore, increasing the angular resolution to $0\farcs08$ would imply incrementing the observing time by a factor of 2.5, therefore making such an observational program hardly feasible. Observations of more optically thin lines, such as ^{13}CO $J = 3$–2, could potentially better trace the perturbations in the gas density caused by the vortex. However, we find that achieving the required signal-to-noise ratio on this line would require more than 15 hr of integration time on source.
3. To measure the velocity gradient across the vortex, the observations should have a velocity resolution at least $3\times$ higher than the amplitude of the velocity perturbations induced by the vortex. We find that the velocity variations associated with the vortex can be comparable to the sound speed in the gas, which, for typical temperature values, varies between 0.3 and 0.6 km s^{-1}. Our simulations show that a velocity resolution of 0.1 km s^{-1} provides the best compromise between the need to spatially resolve the vortex kinematics and that of achieving a sufficiently high signal-to-noise ratio.
4. Finally, we find that the disk inclination plays an important role in the capability of investigating the vortex kinematics. A low disk inclination ($i < 30°$) will cause a smaller projection of the gas velocity along the line of sight and weaker vortex signatures. A high disk inclination ($i > 60°$) might cause the emission from the vortex to be absorbed by the outermost disk regions. The best target candidates should therefore be those disks characterized by moderate inclinations. At the same time, we find that the azimuthal position of the vortex in the moment maps is related to the detection of the asymmetric feature in the gas line moment, but the effect is still unclear. This may be figured out in our future work.

One future study is to investigate the signatures of vortices in a background disk flow that is eccentric. Such configurations can be produced if the planet is quite massive or the disk contains a binary system.

We thank the referee for the detailed comments that improved the presentation of this paper significantly. Part of this work was performed at the Aspen Center for Physics, which is supported by National Science Foundation grant PHY-1607611. This work is supported by the National Natural Science Foundation of China (grant Nos. 11773081 and 11661161013), the CAS Interdisciplinary Innovation Team, and the Foundation of Minor Planets of Purple Mountain Observatory. The financial support provided by the UCAS (UCAS[2015]37]) Joint PhD Training Program and LANL/CSES is acknowledged. AI acknowledges support from the National Science Foundation through grant No. AST-1715719 and the National Aeronautics and Space Administration through grant No. NNX15AB06G. HL and SL acknowledge support from the National Aeronautics and Space Administration through grant No. 80HQTR18T0061 and the Center for Space and Earth Science at LANL.

Software: LA-COMPASS (Li et al. 2005, 2008), RADMC-3D v0.41 (Dullemond 2012), CASA ALMA pipeline 5.0.0 (McMullin et al. 2007).

ORCID iDs

Andrea Isella https://orcid.org/0000-0001-8061-2207
Hui Li https://orcid.org/0000-0003-3556-6568
Shengtai Li https://orcid.org/0000-0002-4142-3080
Jianghui Ji https://orcid.org/0000-0002-9260-1537

References

Adam, J. 1990, A&A, 240, 541
Barge, P., & Sommeria, J. 1995, arXiv:astro-ph/9501050
Birnstiel, T., Dullemond, C. P., & Pinilla, P. 2013, A&A, 550, L8
Boehler, Y., Ricci, L., Weaver, E., et al. 2018, ApJ, 853, 162
Boehler, Y., Weaver, E., Isella, A., et al. 2017, ApJ, 840, 60
Brauer, F., Dullemond, C., & Henning, T. 2008, A&A, 480, 859
Bruderer, S., van der Marel, N., van Dishoeck, E. F., & van Kemepn, T. A. 2014, A&A, 562, A26
Casassus, S., Wright, C. M., Marino, S., et al. 2015, ApJ, 812, 126
Chiang, E., & Goldreich, P. 1997, ApJ, 490, 368
Chiang, E., & Youdin, A. 2010, AREPS, 38, 493
Dullemond, C. 2012, RADMC-3D: A multi-purpose radiative transfer tool, Astrophysics Source Code Library, ascl:1202.015
Flaherty, K. M., Hughes, A. M., Rose, S. C., et al. 2017, ApJ, 843, 150
Flaherty, K. M., Hughes, A. M., Teague, R., et al. 2018, ApJ, 856, 117
Follette, K. B., Grady, C. A., Swearingen, J. R., et al. 2015, ApJ, 798, 132
Frank, J., King, A., & Raine, D. 2002, Accretion Power in Astrophysics (Cambridge: Cambridge Univ. Press)
Fu, W., Li, H., Lubow, S., & Li, S. 2014a, ApJL, 788, L41
Fu, W., Li, H., Lubow, S., Li, S., & Liang, E. 2014b, ApJL, 795, L39
Geers, V., Pontoppidan, K., Van Dishoeck, E., et al. 2007, A&A, 469, L35
Hartmann, L., Calvet, N., Gullbring, E., & D'Alessio, P. 1998, ApJ, 495, 385
Isella, A., Guidi, G., Testi, L., et al. 2016, PhRvL, 117, 251101
Isella, A., Natta, A., Wilner, D., Carpenter, J. M., & Testi, L. 2010, ApJ, 725, 1735
Isella, A., Pérez, L. M., Carpenter, J. M., et al. 2013, ApJ, 775, 30
Isella, A., & Turner, N. J. 2018, ApJ, 860, 27
Jin, S., Li, S., Isella, A., Li, H., & Ji, J. 2016, ApJ, 818, 76
Li, H., Colgate, S., Wendroff, B., & Liska, R. 2001, ApJ, 551, 874
Li, H., Finn, J., Lovelace, R., & Colgate, S. 2000, ApJ, 533, 1023
Li, H., Li, S., Koller, J., et al. 2005, ApJ, 624, 1003
Li, H., Lubow, S., Li, S., & Lin, D. N. 2008, ApJL, 690, L52
Liu, S., Ricci, L., Isella, A., Li, H., & Li, S. 2018, AAS Meeting, 231, 342.15
Lovelace, R., Li, H., Colgate, S., & Nelson, A. 1999, ApJ, 513, 805
McMullin, J., Waters, B., Schiebel, D., Young, W., & Golap, K. 2007, adass XVI, 376, 127
Miranda, R., Li, H., Li, S., & Jin, S. 2017, ApJ, 835, 118
Muto, T., Tsukagoshi, T., Momose, M., et al. 2015, PASJ, 67, 122
Ou, S., Ji, J., Liu, L., & Peng, X. 2007, ApJ, 667, 1220
Pérez, L. M., Isella, A., Carpenter, J. M., & Chandler, C. J. 2014, ApJL, 783, L13
Pérez, S., Casassus, S., & Benítez-Llambay, P. 2018, MNRAS, 480, L12
Pinte, C., Dent, W. R. F., Ménard, F., et al. 2016, ApJ, 816, 25
Pollack, J. B., Hollenbach, D., Beckwith, S., et al. 1994, ApJ, 421, 615
Pollack, J. B., Hubickyj, O., Bodenheimer, P., et al. 1996, Icar, 124, 62
Regály, Z., Sándor, Z., Csomós, P., & Ataiee, S. 2013, MNRAS, 433, 2626
Shakura, N. I., & Sunyaev, R. A. 1973, A&A, 24, 337
Teague, R., Henning, T., Guilloteau, S., et al. 2018, ApJ, 864, 133
van der Marel, N., Pinilla, P., Tobin, J., et al. 2015, ApJL, 810, L7
van der Marel, N., Van Dishoeck, E. F., Bruderer, S., et al. 2013, Sci, 340, 1199
Weaver, E., Isella, A., & Boehler, Y. 2018, ApJ, 853, 113
Weidenschilling, S. 1977, MNRAS, 180, 57
Weingartner, J. C., & Draine, B. 2001, ApJ, 548, 296
Zhu, Z., Stone, J. M., Rafikov, R. R., & Bai, X.-n. 2014, ApJ, 785, 122
Zubko, V., Krelowski, J., & Wegner, W. 1998, MNRAS, 294, 548